Coincident electrofission of ^{238}U at $q \approx 0.26$, 0.40, and 0.55 fm^{-1}

K. A. Griffioen,* P. J. Countryman, K. T. Knöpfle,† K. Van Bibber, and M. R. Yearian
Department of Physics and High Energy Physics Laboratory, Stanford University, Stanford, California 94305

J. G. Woodworth and D. Rowley
Lawrence Livermore National Laboratory, Livermore, California 94550

J. R. Calarco
Department of Physics, University of New Hampshire, Durham, New Hampshire 03824
(Received 27 May 1986)

We have measured the coincidence cross sections ^{238}U(e,e′f) at three values of momentum transfer ($q \approx 0.26$, 0.40, and 0.55 fm^{-1}) over the range from 5 to 23 MeV in excitation energy; these values of q correspond approximately to the first maxima of the electric dipole, quadrupole/monopole, and octupole form factors, respectively. The angular distribution of fission fragments is peaked along the direction of q near fission threshold, indicating the dominance of $K=0$ states, but becomes isotropic above 10 MeV. We have integrated our cross sections over fission angle and compared them to recent calculations of multipole strength derived in the quasiparticle random phase approximation. Using model-dependent form factors generated from the Tassie model and the quasiparticle random phase approximation, we have extracted strength functions for the lowest electric multipoles. The deduced $E1$ strength agrees well with photofission results for reasonable choices of the model form factors. The $E2/E0$ distribution displays resonant structures at 10 and 13 MeV which agree in position with the collective $E2$ and $E0$ strength, respectively, predicted in the quasiparticle random phase approximation. If we make such an assignment for the multipolarity of these two structures, the observed $E0$ strength agrees with the theoretical prediction, whereas the $E2$ strength is low by a factor of 2—3. Higher order multipoles also contribute substantially to the cross section at our highest value of q.

I. INTRODUCTION

Most of the experimental evidence for the giant monopole (GMR), quadrupole (GQR), and octupole (GOR) resonances comes from observations in which large backgrounds dwarf the resonant contribution.[1] This background renders these measurements insensitive to multipole strength that is not well localized in excitation energy. The broad overlapping nature of the multipole resonances further complicates attempts to identify them.

Two most widely used reactions for these studies have been the inelastic scattering of alpha particles and electrons. Alpha particles are useful because they predominantly excite isoscalar resonances. Therefore, the giant dipole resonance (GDR) will not interfere with the isoscalar GMR and GQR. Both inclusive (α,$\alpha'f$) (Refs. 2 and 3) and coincidence (α,α') (Refs. 4—10) experiments on uranium display a large continuum background due to multistep processes which is not fully understood. Electrons, on the other hand, although exciting isoscalar and isovector resonances equally, interact with the nucleus in a well-understood and simple manner. Electron scattering proceeds almost exclusively through the exchange of a single virtual photon. However, the inclusive scattering (e,e′) (Ref. 11) at forward angles and low q suffers from the large radiative tail of the elastic scattering which accounts for at least 95% of the cross section in the giant-resonance region. Although one can, in principle, calculate the radiative tail to any degree of precision, in practice the presence of even a small non-target-related background leads to large systematic uncertainties. One must therefore parametrize the shape, fit it to the observed tail in a region devoid of inelastic excitation, and extrapolate to the region of the giant resonances. This is particularly difficult for high-Z nuclei with large inelastic scattering contributions throughout a full range of excitation energy.

Inclusive electrofission experiments ^{238}U(e,f) (Refs. 12—19) do not provide the resonant strength directly; they record a convolution of that strength with a spectrum of virtual photons produced by the electron's field. The electric dipole contribution dominates in these cross sections, making an extraction of $E2$ strength very sensitive to the absolute magnitude of the cross section and the precise form of the theoretical virtual photon spectrum used for unfolding. No one yet knows either of these quantities to sufficient accuracy to make a realistic determination of the $E2$ strength.[19] The various experiments yield $E2$ strengths in the fission channel ranging from 0% to 70% to a full sum rule. In the course of our coincidence experiment we have measured (e,f) cross sections between 45 and 120 MeV (Ref. 19) and have compared these with calculations incorporating the most recent distorted wave calculations of the virtual photon spectra which include the finite nuclear size.[20] These results are consistent with the coincidence results presented below, but shed no new light on the problem.

Demanding a coincidence between the scattered electron and decay particle alleviates many of the problems

with inclusive electron scattering experiments. The large radiative tail from the elastic scattering disappears, and the coincidence spectrum becomes free of background. Thus, these exclusive measurements hold the promise of accurately determining multipole excitation functions, even when the strength is not concentrated in a resonance, as well as giving a precise account of the nuclear decay in the continuum. Coincidence experiments have only recently become possible with the advent of a new class of high-duty-factor electron accelerators. A group at the University of Illinois has performed the first (e,e'f) measurement on ^{238}U.[21] In the present experiment we have extended their measurements to higher momentum transfer q and excitation energy ω. This paper expands an earlier letter concerning our work and condenses an unpublished report of the same.[22]

II. ELECTRON SCATTERING FORMALISM

Electrons of initial relativistic momentum $\mathbf{k}$ bombard a thin uranium target. Those scattered at $\theta_{e'}=40°$, having momentum $\mathbf{k}'$, enter a magnetic spectrometer for analysis. The virtual photon produced in scattering transfers momentum $q=k-k'$ and energy $\omega=k-k'$ to the uranium nucleus, thereby exciting the giant resonances. Because the recoil kinetic energy of the heavy target nucleus is negligible, essentially all of the energy ω goes into internal excitation. The subsequent decay of the giant resonances in ^{238}U proceeds almost exclusively[23] by fission or neutron emission. We have measured this fission decay at various angles in the present experiment. We assume that the decay of the giant resonances is independent of the electroexcitation mechanism which formed them, and therefore that these two processes can be treated separately.

A. Electroexcitation

Kleppinger and Walecka[24] have derived a general expression for the coincidence electron scattering cross sections in the plane-wave Born approximation (PWBA). For a single resonance with spin and parity λ^{π} in a nucleus with a 0^+ ground state, we choose to write

$$\frac{1}{\sigma_M}\frac{d^3\sigma_f}{d\omega\, d\Omega_{e'} d\Omega_x}=(V_C\,|F_C|^2+V_T\,|F_T|^2)\sum_k A_k P_k(\cos\theta)+V_{CT}\mathrm{Re}F_C^* F_T\sum_k B_k P_k^1(\cos\theta)\cos\phi$$
$$+V_{TT}\,|F_T|^2\sum_k C_k P_k^2(\cos\theta)\cos 2\phi\ , \tag{1}$$

in which σ_M is the Mott cross section given by

$$\sigma_M=\frac{Z^2\alpha^2\cos^2(\theta_{e'}/2)}{4E_0^2\sin^4(\theta_{e'}/2)}\ ,$$

E_0 is the incident beam energy, Z is the nuclear charge, α is the fine structure constant, V_C, V_T, V_{CT}, and V_{TT} are kinematic factors, $|F_C|^2$ and $|F_T|^2$ are the Coulomb and transverse form factors, P_k^m are the associated Legendre polynomials, A_k^m, B_k^m, and C_k^m are the angular correlation coefficients of the decay, and the summation index k runs from 0 to 2λ constrained by the fact that P_k^m must be defined. We use the coordinate system in which $\hat{\mathbf{z}}=\hat{\mathbf{q}}$ and $\hat{\mathbf{y}}=\hat{\mathbf{k}}\times\hat{\mathbf{k}}'$, whereas Kleppinger uses a system with $\hat{\mathbf{y}}$ and $-\hat{\mathbf{x}}$ exchanged.[25] The form factors are tied to the Coulomb and transverse multipole operators by the relations[26]

$$|F_C|^2=|\langle\lambda||\hat{M}_\lambda(q)||0\rangle|^2\ ,$$
$$|F_T|^2=|\langle\lambda||\hat{T}^{\mathrm{el}}_\lambda(q)||0\rangle|^2\ . \tag{2}$$

The Coulomb matrix elements depend on the radial transition charge density $\rho^\lambda_{\mathrm{tr}}(r)$ and the spherical Bessel functions $j_\lambda(qr)$:

$$\langle\lambda||\hat{M}_\lambda(q)||0\rangle=\int_0^\infty j_\lambda(qr)\rho^\lambda_{\mathrm{tr}}(r)r^2dr\ . \tag{3}$$

In the low-q limit and also in the hydrodynamic model for collective excitations,[24] the transverse (current) matrix elements are related to the Coulomb elements by

$$\langle\lambda||\hat{T}^{\mathrm{el}}_\lambda(q)||0\rangle=-\left[\frac{\lambda+1}{\lambda}\right]^{1/2}\frac{\omega}{q}\langle\lambda||\hat{M}_\lambda(q)||0\rangle\ . \tag{4}$$

The angular correlation coefficients A_k depend on the multipolarity of the transition and on the decay mechanism. Once these are known, however, the coefficients B_k and C_k can be calculated directly. For comparison with a continuum spectrum, e.g., the giant resonance region with overlapping resonances, Eq. (1) must be summed over multipolarity.

For discrete states, the transition charge density results directly from a Fourier transform of the experimental form factor σ/σ_M. Such a transformation is possible because these states are narrow and easily identified, even at large momentum transfers where the cross sections are small. The broad resonances in the continuum, on the other hand, overlap with resonances of other multipolarities. In addition, the idea of localized resonances with well-defined shapes is not well founded; one should speak more precisely of a strength function $dB(B\lambda,\omega)/d\omega$ which may be broadly distributed in excitation energy. Although measurements of the continuum response over a large range of q would permit the determination of both the strength function and the transition densities of all multipolarities in a self-consistent and unambiguous way, this goal is a long way off, in practice. In the present work, which was limited to only three values of q, we must assume some model for $\rho^\lambda_{\mathrm{tr}}(r)$ and calculate the q dependence of the form factors.

Fortunately, at low momentum transfers the form fac-

tors depend only on average values of the charge distribution. For reasonably small values of q, qr will be small compared to unity wherever $\rho_{\rm tr}^{\lambda}(r)$ is nonzero. Therefore we can write

$$j_\lambda(qr) \approx \frac{q^\lambda r^\lambda}{(2\lambda+1)!!} , \tag{5}$$

and the form factor will only depend on an average property of the transition density, the transition radius:

$$R_{\rm tr}^{\lambda} = \left[\int_0^\infty r^{\lambda+2} \rho_{\rm tr}^{\lambda}(r) dr \Big/ \int_0^\infty r^2 \rho_{\rm tr}^{\lambda}(r) dr \right]^{1/\lambda} . \tag{6}$$

The transition strength of a particular state is also defined in this low-q region where the momentum transfer factors out of the integral:

$$\begin{aligned} B(E\lambda) &= \lim_{q\to 0} \{ [(2\lambda+1)!!]^2 q^{-2\lambda} | \langle \lambda || \hat{M}_\lambda(0) || 0 \rangle |^2 \} \\ &= \left| \int_0^\infty r^{\lambda+2} \rho_{\rm tr}^{\lambda}(r) dr \right|^2 . \end{aligned} \tag{7}$$

Because the volume integral of the transition charge density vanishes for the compressional monopole vibration, it must be treated as a separate case:

$$\begin{aligned} B(E0) &= \lim_{q\to 0} [4\pi 36 q^{-4} | \langle 0 || \hat{M}_0(q) || 0 \rangle |^2] \\ &= 4\pi \left| \int_0^\infty r^4 \rho_{\rm tr}^{0}(r) dr \right|^2 . \end{aligned} \tag{8}$$

In heavy nuclei like uranium the plane wave Born approximation fails due to the large Coulomb force, thus making the distorted wave Born approximation (DWBA) necessary for all calculations. The distorted waves mix the Coulomb and transverse contributions to the cross section and fill in the minima of the form factors. In this case the matrix elements depend on E_0 and $\theta_{e'}$ as well as on q.

B. Fission decay

In a deformed nucleus such as uranium (prolate), a new quantum number K arises from the projection of the total angular momentum onto the body-fixed symmetry axis. The quantum mechanical wave functions for such a system are those of a symmetric rotor. These are the rotational wave functions $D_{MK}^{J}(\alpha,\beta,\gamma)$ for which (α,β,γ) are the Euler angles required to rotate the lab system to the body fixed system. Since fission fragments are presumed to emerge along the body-fixed symmetry axis,[27] the differential cross section as a function of angle is proportional to

$$| D_{MK}^{J}(\alpha,\beta,\gamma) |^2 \sin\beta \, d\beta \, d\alpha .$$

The q direction defines the z axis for the fissioning system; therefore, $\beta \equiv \theta_f$ and $\sin\beta \, d\beta \, d\alpha \equiv d\Omega_f$, and

$$\begin{aligned} \frac{d\sigma}{d\Omega_f} &\propto | D_{MK}^{J}(\alpha,\beta,\gamma) |^2 = | d_{MK}^{J}(\theta_f) |^2 \\ &\equiv \frac{2}{2J+1} W_{MK}^{J}(\theta_f) . \end{aligned} \tag{9}$$

The angular distribution functions $W_{MK}^{J}(\theta_f)$ are normalized such that their integral over all solid angle is unity. Table I lists these angular distribution functions for various values of J and K. In the PWBA limit M must be exactly zero. The contribution from $M=0$ states at the energies of this experiment are expected to be small.

These angular correlation coefficients in the framework of the electron scattering formalism can be expressed as

$$W_{MK}^{J}(\theta_f) = \sum_{k=0}^{2J} D_k P_k(\cos\theta_f) , \tag{10}$$

in which the coefficients D_k are nonzero only when k is even due to the symmetry imposed by fission fragments being emitted back to back. Equation (10) determines the coefficients of Eq. (1) for a state with particular values of J and K.

III. EXPERIMENTAL SETUP

A. Spectrometer

The inelastically scattered electrons were analyzed in a 91 cm double-focusing magnetic spectrometer,[28] instrumented with 24 NE102 plastic scintillators in combination with an NE102 backing counter and a lucite Čerenkov counter. The 24 counters, of dimension $0.95 \times 0.95 \times 10.2$ cm, overlapped each other by a third, forming a total of 47 channels. The momentum acceptance of the system was $\Delta p/p = 0.04$, implying better than 200 keV resolution per channel for electron beams below 200 MeV delivered by the Stanford Superconducting Recyclotron.[29]

The solid angle-efficiency product was determined by measuring the elastic scattering from a ^{12}C target of known thickness: Indeed, taking the nominal solid angle of 3.6 msr from ray-tracing showed the focal plane array to have an efficiency of $[(100 \pm 5)\%]$.

We determined the location of the focal plane, the dispersion calibration of the detectors, and the final energy calibration using a combination of actual electron scattering data on ^{12}C and calculations using the program

TABLE I. The angular correlation functions $W_{0K}^{J}(\theta)$.

J	$K=0$	$K=1$	$K=2$	$K=3$
0	$\frac{1}{2}$			
1	$\frac{3}{2}\cos^2\theta$	$\frac{3}{4}\sin^2\theta$		
2	$\frac{5}{8}(3\cos^2\theta-1)^2$	$\frac{15}{4}\cos^2\theta\sin^2\theta$	$\frac{15}{16}\sin^4\theta$	
3	$\frac{7}{8}(5\cos^3\theta-3\cos\theta)^2$	$\frac{21}{32}(5\cos^2\theta-1)^2\sin^2\theta$	$\frac{105}{16}\cos^2\theta\sin^4\theta$	$\frac{35}{32}\sin^6\theta$

TRANSPORT (Ref. 30) and ray-tracing codes.

The calculated dispersion of each of the 47 spectrometer channels relies on the incorrect assumption that each channel is exactly 0.32 cm wide. To allow for size variations, we have assigned a relative efficiency, close to unity, to each channel. Measurements of these relative efficiencies were made from the smooth portions of the ^{12}C(e,e') radiative tail. We fitted the observed scattering spectrum to the theoretical radiative tail plus a $1/E$ background. The form of the background results from the assumption that each detector sees the same non-target-related background count rate. The normalized spectrum of these events (counts/MeV/μC) will have a $1/\Delta E_i$ dependence, for which ΔE_i is the energy dispersion of an individual element in the focal plane. Since ΔE_i is proportional to the mean energy of electrons analyzed in detector i, the background varies as $1/E$. The relative efficiencies were defined as the ratio of counts in a particular channel compared to the smooth fitted curve. Even channels, which correspond to overlap between two physical scintillators, had efficiencies less than unity. Odd channels, which correspond to the middle third of each scintillator, had efficiencies larger than unity. The efficiency correction preserved the number of total counts recorded in the focal plane and, in general, merely redistributed counts from the overlap channels into their nearest neighbors.

The scattering angle of 40° proved to be a compromise between high coincidence counting rates at small angles (due to the rapidly rising Mott cross section) and high momentum transfer for a fixed beam energy at large angles. This was still far enough forward in angle such that only electric multipoles contributed significantly to the cross sections.

B. Parallel plate avalanche counters

Parallel plate avalanche counters (PPAC's) have been demonstrated to provide fission fragment identification in an intense electron background,[31] an environment which easily overloads scintillators and solid state detectors. Furthermore, fission fragments rapidly damage solid state detectors, whereas PPAC's are impervious to such damage.

We have used arrays of PPAC's in two configurations (shown in Fig. 1) during the present experiment. Although the six detectors in Fig. 1(a) are arranged symmetrically about the beam axis, they see different angles with respect to the direction of momentum transfer q. Table II lists the mean angle with respect to q and the deduced solid-angle efficiency product for each PPAC in the two configurations.

Each rectangular PPAC was roughly 4 cm$\times$8 cm in size and consisted of an aluminum cathode embedded in a lucite body and a 2 μm aluminized Mylar anode mounted on an aluminum frame. The anode and cathode were separated by 3 mm. A second Mylar window retained the propane gas which constantly flowed through the PPAC's. This window bulged slightly at the operating pressure of 12 Torr; however, the anode window remained parallel to the cathode at all points. A positive voltage of $\approx$650 V produced an excellent signal-to-noise ratio.

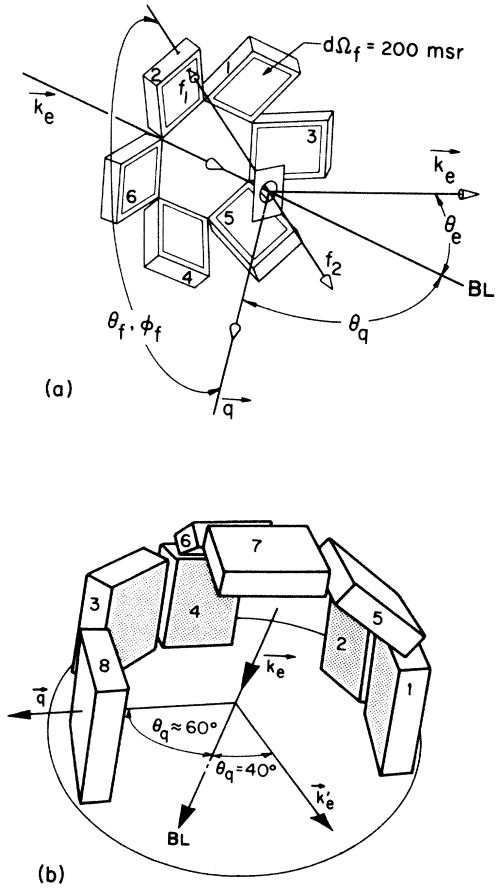

FIG. 1. The PPAC configurations used in the present experiment, for (a) the first and third runs, and (b) the second run.

Leading edge discriminators were used for the fast ($\leq$5 ns rise time after transmission through 100 m of 50 Ω coaxial cable) PPAC signals.

The solid angles of the PPAC's were measured in two ways. We placed a ^{252}Cf source at the target position and recorded relative counting rates for the PPAC's with respect to a solid state counter of precisely determined solid angle. This method, when applied to the array of Fig. 1(a), agreed within the accuracy of the measurement (5%) with a geometrical determination of the solid angle deduced by numerical integration over the rectangular faces of the detectors (accurate again to 5%); this agreement was assurance of the 100% efficiency of the avalanche counters. For the arrangement of Fig. 1(b) the source test was not accurate for the detectors 3', 5', 6', and 7' since the fission fragment distribution of the ^{252}Cf source falls off at small angles with respect to the plane of the foil. Nor could the geometrical results be relied upon entirely, because detectors 3' and 7' were partially shadowed by the target in the actual experiment. Hence, we determined relative solid angles using the accidental coincidence events collected during the experiment; these will have the angular distribution of the singles ^{238}U(e,f) cross section which is known to be isotropic[13–15] at the beam energies of this experiment. We then obtained the absolute solid angles by normalizing to the results of the detec-

TABLE II. Angular positions of the centers of the PPAC's with respect to a momentum transfer direction of 65° from the beam axis expressed in the coordinate system with $\hat{z}=\hat{q}$ and $\hat{y}=\hat{k}\times\hat{k}'$. Detectors used in the second and third experimental runs are indicated with primes and double primes, respectively. Deduced solid angle-efficiency products are also given for each detector.

PPAC	$\bar{\theta}$ (deg)	$\bar{\phi}$ (deg)	$\Delta\Omega$ (msr)
1	128	206	202
2	82	227	197
3	170	270	193
4	85	315	195
5	128	333	197
6	62	272	200
1′	174	275	155
2′	140	271	150
3′	55	270	115
4′	87	271	152
5′	133	184	202
6′	90	220	234
7′	85	187	113
1″	170	270	169
2″	128	206	121
3″	82	227	182
4″	62	272	142
5″	85	315	146
6″	128	333	211

tor for which the ^{252}Cf source test and the geometrical calculations agreed. Again, the estimated uncertainty is 5%.

C. Other details

The targets employed in the measurements consisted of 536, 454, 455, and 369 μg/cm^2 of depleted uranium between layers of 40 μg/cm^2 carbon. The carbon not only reduced target oxidation, but also provided the necessary thermal emissivity to carry off the energy from the electron beam. We deduced the thicknesses with 4% accuracy using Rutherford scattering of 12 MeV alpha particles produced at the Lawrence Livermore National Laboratory Cyclograaff facility. These numbers agreed with estimates made during target fabrication.

A toroid current monitor 20 cm upstream from the scattering chamber integrated the beam current. We calibrated the integrator by drawing a known current through a wire which passed through the toroid. The integration system proved reliable to 2% accuracy in the final data-taking run.

We have taken the present data in three separate runs, the first and the third using the configuration of Fig. 1(a) and the second using the array of Fig. 1(b). These data correspond to incident beam energies of 80.3 and 118.4 MeV in the first run, 82.5, 120.7, and 163.8 MeV in the second run, and 81.6, 119.1, and 159.9 MeV in the third run, and cover a number of overlapping spectrometer settings spanning 5—23 MeV in excitation energy. Typical beam currents were 10—40 μA, and with duty factors of 50%, except at the highest energies.

IV. DATA REDUCTION

A. Cross section

For each coincident event, a CAMAC time-to-digital converter recorded the time difference between the electron and the fission signals. The corresponding spectrum (see Fig. 2) shows a large peak due to true coincidences, typically 8 ns wide [full width at half maximum (FWHM)], on top of a flat background. The electronic gating of the coincidence circuitry limits the background plateau to 100 ns in duration. The events in the region away from the true coincidence peak allow for an accurate subtraction of accidental coincidences from true events.

The number of true events divided by the energy width of the spectrometer channel, the solid angles of the fission counter and the spectrometer, the target thickness, and the integrated charge yields the triply differential cross section, which is a function of excitation energy and fission angle. We have divided the measured number of fission fragments by 2 so that the deduced cross sections reflect probabilities for fission rather than for fission-fragment production (two per fission). Since the dispersion of the spectrometer is not uniform, we rebinned the data into equal-energy intervals 200 keV wide.

Figure 3 shows the resulting cross sections for an incident electron energy of 118.4 MeV using the PPAC configuration of Fig. 1(a). The electrofission cross section rises dramatically at 5.9 MeV once the fission barrier is reached. At 6.14 MeV neutron emission begins to compete with fission, causing the cross section to drop sharply. The result is a prominent peak at threshold. The angular distribution of fission fragments in the threshold region is clearly peaked along the direction of **q**. The spectra at higher excitation energies reflect the giant-resonance structure modified by the probability for giant resonance decay by fission. The fission probability rises sharply near 12 MeV, where second chance fission (emission of a neutron and then subsequent fission decay) becomes possible, and near 18 MeV at the third chance fission threshold.

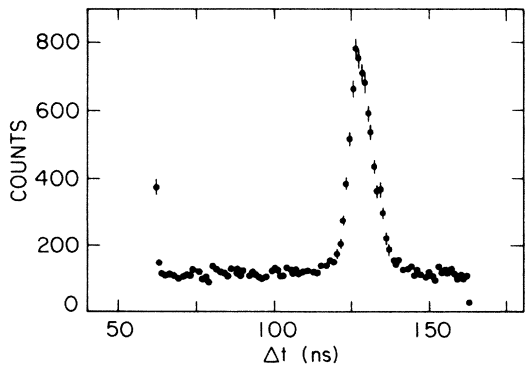

FIG. 2. The time spectrum for coincidence events. True coincidences in the large peak sit on a flat background of random coincidences.

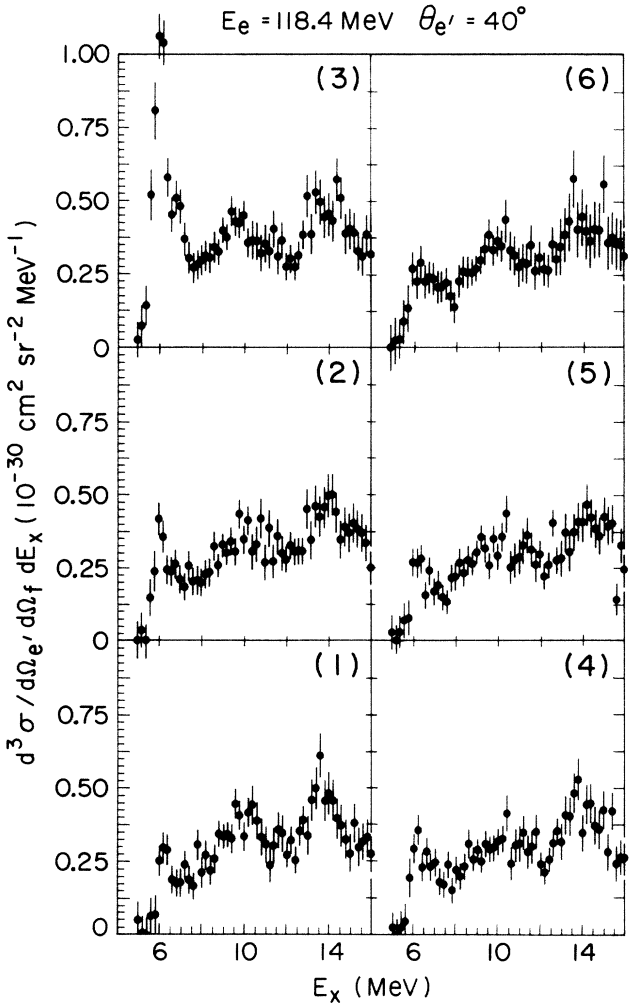

FIG. 3. Triply differential cross sections $d^3\sigma_f/d\Omega_e d\Omega_f d\omega$ at six different fission angles (see Table II) for an incident energy of 118.4 MeV.

B. Radiative corrections

Although the coincidence requirement removes the radiative tail due to elastic scattering, the inelastic spectrum itself is subject to radiative corrections. The measured cross section for a discrete inelastic state (integrated over an energy interval ΔE which starts at the energy of the inelastic state and extends to higher energy loss) takes the form

$$\frac{d\sigma(\Delta E)}{d\Omega}=\left[\frac{d\sigma_R}{d\Omega}\right](1-\delta_S)\,,$$

with $d\sigma_R/d\Omega$ being the actual inelastic cross section and δ_S the Schwinger correction. Maximon[32] has given this correction as

$$\delta_S=\frac{2\alpha}{\pi}\left[\left[\log\frac{\sqrt{E_1E_2}}{\Delta E}-\frac{13}{12}\right]\left[\log\frac{q^2}{m^2}-1\right]+\frac{17}{36}+\frac{1}{4}\log^2\frac{E_1}{E_2}\right]\,, \tag{11}$$

in which E_1 and E_2 are the incident and scattered electron energies, respectively, ΔE is the integration interval, and m is the electron mass. Equation (11) includes four second-order Feynman diagrams: soft photon emission before and after scattering, the vertex correction, and the vacuum polarization. Hard photon emission is simply bremsstrahlung, which, along with Landau straggling, is negligible for our setup with thin targets and no intervening windows between spectrometer and scattering chamber. In order to include many of the higher order diagrams in the radiative correction, we have used $e^{-\delta_S}$ rather than $1-\delta_S$ as the correction factor.

We have applied the Schwinger correction for discrete states to the present case of continuous inelastic states using a method developed by Crannell.[33] This technique assumes that Eq. (11) is exact and that the statistical errors of each successive small correction to a channel add in quadrature. The radiative correction increases the magnitude of the coincidence cross section near threshold by 20%, but at 20 MeV the modified cross section is larger by only 3—5%.

We performed the third of the three runs with careful attention to the absolute normalization of the cross sections. The data from the first two runs proved to be slightly smaller in magnitude at equivalent fission angles than the final data set. We have traced this difference back to a systematic problem in charge integration during the first two runs. Nevertheless, the absolute cross section between runs agrees to within 20%. In order to produce a self-consistent data set, we have scaled the first two runs upward slightly ($<20\%$) to agree in magnitude with the final data set. We also took into account the variations in beam energy between the three runs by scaling by the ratio of Mott cross sections (i.e., the nominal energy 80.3 MeV results from actual runs at 80.3, 82.5, and 81.6 MeV). This assumes that the nuclear form factor is not changing rapidly over a small change in beam energy. For the three runs, the relative cross sections between 80, 120, and 160 MeV incident energies as a function of excitation energy agreed to better than 5%.

C. Angular correlations

In order to obtain giant resonance strengths, we must integrate the triply differential cross sections over fission angle. The analysis of the fission fragment angular distribution given in Sec. II predicts a possible dependence on ϕ, the azimuthal angle with respect to $\mathbf{q}$. Within our statistical accuracy of 7%, we saw no ϕ dependence between detectors with roughly the same values of θ. Hence, we were satisfied to fit all of our angular distributions to the form

$$\frac{d^3\sigma_f}{d\omega\, d\Omega_{e'}\, d\Omega_f}=\sum_k a_k P_k(\cos\theta_f)\,, \tag{12}$$

in which a_k are constants which depend only on excitation energy, P_k are Legendre polynomials, and θ_f is the polar angle between $\mathbf{q}$ and the fission axis. Odd terms do not contribute to the sum because fission fragments emerge back to back. We omit higher order polynomials due to the predominance of low order multipolarities in

our data. Fits using coefficients up to a_4 provided reasonable results, whereas the fit which included a_6 displayed wild oscillations in the a_4 and a_6 coefficients as a function of excitation energy, indicating that the data do not contain enough information to accurately extract a_6. Hence, we have restricted ourselves to determining a_0, a_2, and a_4 only.

We averaged both P_2 and P_4 over the solid angle subtended by the PPAC's for each value of excitation energy, taking care to rotate our coordinate system with the changing direction of $\mathbf{q}$. (At fixed beam energy, θ_f varied from 50° to 70° as ω moved from threshold to 25 MeV.) We then fitted the data to these new averaged functions using a least-squares method[34] for generalized functions which properly calculates associated errors in the coefficients a_0, a_2, and a_4 as well as an overall χ^2. The χ^2 per degree of freedom in each of these fits was near unity.

Figures 4—6 show the results of these angular fits using all of the triply differential cross section measured in the three runs. The data at each energy show a marked anisotropy near threshold but an isotropic distribution above 10 MeV. One expects deviations from isotropy only near the barrier where fission will proceed from the compact

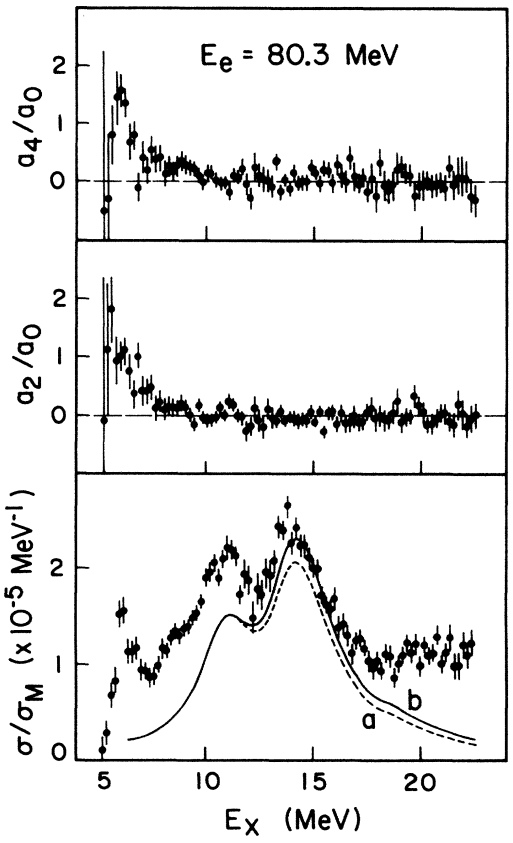

FIG. 4. Results of the least-squares fit of the fission-fragment angular distribution at 80.3 MeV. The angular correlation coefficients a_0, a_2, and a_4 are described in the text. The bottom panel is the experimental form factor, along with two calculations of the $E1$ contribution. These were obtained from the Saclay (Ref. 35) photofission data and (a) Tassie model and (b) QRPA form factors.

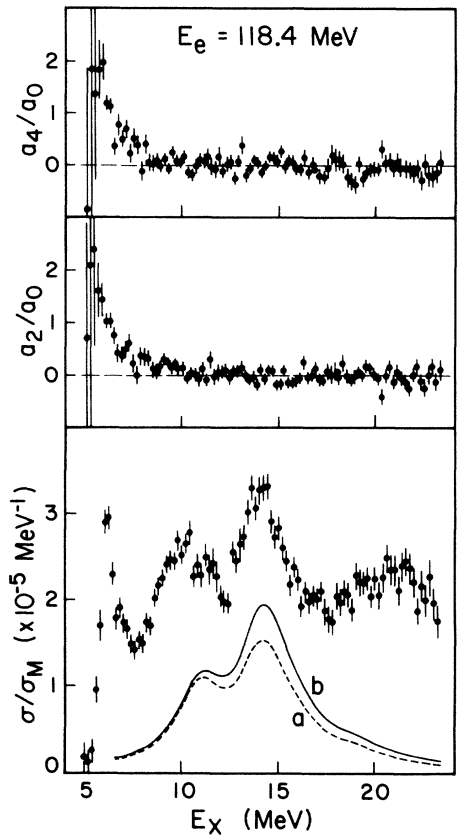

FIG. 5. Results of the least-least-squares fit of the fission fragment angular distribution at 118.4 MeV.

ground state shape to binary fragments through relatively few transition states at the saddle point.[35] The bottom curve of each set is simply $4\pi a_0$ normalized to the Mott cross section; this is the angle-integrated experimental form factor. The curves below the data indicate the $E1$ contribution to the cross section calculated using a strength function deduced from the photofission work at Saclay[36] and either (a) Tassie model or (b) quasiparticle random-phase-approximation (QRPA) form factors. Clearly, the $E1$ component comprises a major portion of the cross section at 80 MeV, but diminishes in importance at 160 MeV.

The peaking of the cross sections along the direction of $\mathbf{q}$ at threshold indicates the dominance of $K=0$ states, as expected from a Gaussian K distribution.[37] Figure 7 shows the angular distribution of fission fragments at threshold. The shaded region, resulting from the angular fit to the data, peaks along the direction of momentum transfer, consistent with the assumption of $K=0$ states. However, at all three energies the shape cannot be fitted to a single value of J. The solid line indicates the angular distribution resulting from equal fractions of the $E0$, $E1$, $E2$, and $E3$ sum rules calculated with Tassie-model form factors. These curves scale roughly with the data, but do not give the correct shape. One might expect better results with less $E0$ strength and more $E2$ and $E3$ strength. With more detailed angular distributions at threshold, one could determine both J and K, but this is not possible

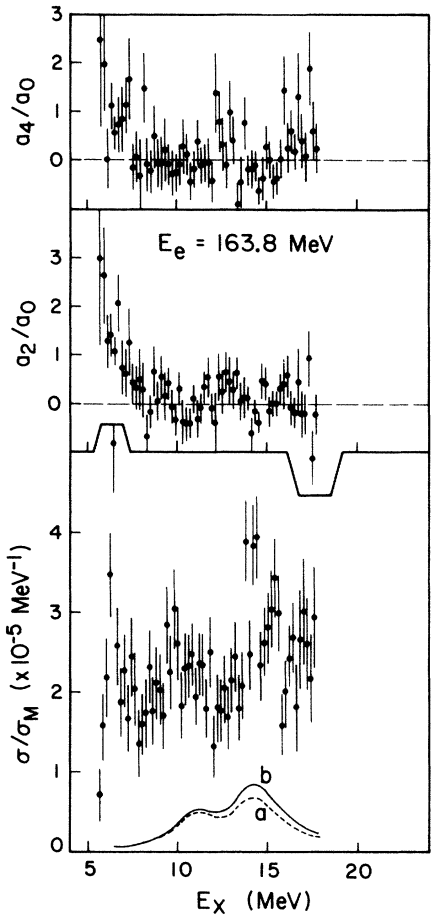

FIG. 6. Results of the least-squares fit of the fission fragment angular distribution at 163.8 MeV.

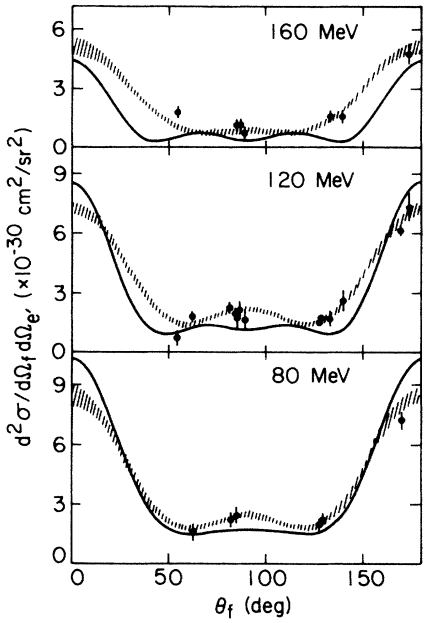

FIG. 7. The angular distribution of fission fragments at threshold. The data points correspond to the triply differential cross sections integrated over $5.5 \leq E_x \leq 6.5$ MeV. The shaded area is the result of the fit to a_0, a_2, and a_4. Although the fit incorporates integrating the angular correlation functions over the detector solid angles, the data points themselves are uncorrected. The solid line corresponds to the cross section resulting from equal fractions of the $E0$, $E1$, $E2$, and $E3$ sum rules at threshold assuming that only $K=0$ states contribute.

with the present data.

At higher excitation energies one could still expect the angular distribution to be determined by J and K of the resonance if K remains a good quantum number as the nucleus proceeds from its mildly prolate ground state shape to the more distended saddle point. This should be true in spite of the fact that fission could proceed through any of a number of allowed transition states with fixed J and K, even though the density of these states is very great. Whether K is actually conserved in processes like these remains an interesting open question. The present data indicate that K is not conserved from giant resonance to scission. The 80 MeV data of Fig. 4, measured at low momentum transfer, are predominantly $E1$ in character. The dipole resonance splits into two components due to the intrinsic deformation of uranium, a $K=0$ mode centered at $E_x=11$ MeV and a $K=1$ mode centered at $E_x=14$ MeV. If these K values were, in fact, conserved through the fission process, one would observe a forward peaking of the cross section at 11 MeV and a peaking at 90° near 114 MeV. Any anisotropy above the second-chance fission barrier ($E_M<12$ MeV) will not be as marked as at lower excitations because K of the giant resonance is probably lost in the initial neutron decay for roughly half of the observed cross section. However, neither above nor below 12 MeV do we see the anisotropy which would have indicated that K is conserved.

V. THEORETICAL PREDICTIONS

Unlike the discrete states, the overlap of many broad resonances in the giant resonance region makes a model-independent extraction of multipole strength difficult. For a data set covering a limited range in q, some assumptions must be made about the transition charge density. We have calculated the electron scattering cross section per unit $B(E\lambda)$ as a function of momentum transfer using a model transition charge density and the distorted wave code FOUBESFIT,[38] which uses a Fourier-Bessel expansion of the transition charge and current densities assuming irrotational flow. The form factors are calculated as a function of effective momentum transfer[38]

$$q_{\text{eff}}=q\left[1+\frac{4}{3}\frac{Z\alpha}{E_0A^{1/3}}\right]. \tag{13}$$

By fitting the measured cross sections to these model-dependent form factors, we have extracted corresponding values of $B(E\lambda)$ for 200 keV (or 1 MeV) intervals in excitation energy from 5 to 23 MeV. The details of the fitting procedure are given in the following subsections and Sec. VI.

A. The Tassie model

The simplest assumption for $\rho_{tr}^{\lambda}(r)$ comes from the hydrodynamic Goldhaber-Teller model[39] extended by Tassie[40] to include multipolarities other than the $E1$ resonance. The assumption of incompressible and irrotational fluid flow leads to the surface-peaked form (for $\lambda \geq 1$)

$$\rho_{tr}^{\lambda}(r) = r^{\lambda-1}\frac{d\rho_0(r)}{dr}, \tag{14}$$

in which λ is the multipolarity of the transition and ρ_0 is the ground-state charge distribution. The hydrodynamic transition density for the monopole vibration is given by[41]

$$\rho_{tr}^{0}(r) = -3\rho_0(r) - r\frac{d\rho_0}{dr}. \tag{15}$$

In the limit of low q, the form factor depends only on the transition radius R_{tr}^{λ} and on no other details.

We have taken a Fermi form

$$\rho_0(r) = \frac{\rho_0}{1+e^{-(r-c_0)/t}} \tag{16}$$

for the ground state charge distribution in uranium with the half-density radius $c_0 = 6.805$ fm and the skin thickness $t = 0.605$ fm from the electron scattering data of Cooper *et al.*[42] and Creswell.[43] The dependence of the form factors on the transition charge radii may therefore be explored conveniently by varying arbitrarily the half-density radius. We have chosen values of $c_{tr}/c_0 = 0.9$, 1.0, 1.1, and 1.24 for which to calculate form factors. [Pitthan *et al.*,[11] in the analysis of their (e,e') data, suggest that the $K=0$ and 1 substates of the dipole resonance have transition radii corresponding to $1.24c_0$ and $0.9c_0$, respectively, reflecting the intrinsic prolate deformation of uranium in its ground state.]

Figure 8 shows the calculated Tassie model dipole form factors corresponding to various values of the transition radius. As c_{tr}/c_0 (and thus the transition radius) decreases, the form factor peaks at a larger momentum transfer and grows in magnitude [note that these curves are normalized to unit $B(E1)$].

Figure 9 shows the $\lambda = 1$–4 Tassie model form factors for $c_{tr}/c_0 = 1$ normalized to a full $E\lambda$ sum rule at $E_x = 10$ MeV for each multipole. Note that at the maximum of the $E\lambda$ form factor, the form factors for $\lambda \pm 1$ are only reduced by a factor of 2 from their maximum values. For the purpose of illustration one may consider the case in which equal fractions of the sum rule strength are present for each multipole at a particular excitation energy. The experimental form factor as a function of q would increase monotonically, or only slowly turn over at large q (as indicated in Fig. 9 for multipolarities up to $\lambda = 4$). In this scenario, any multipole decomposition resulting from reasonably placed values of q will result in a "truncation" error, principally on the strength of the dominant multipole of highest q. For example, the present data were taken at $q \cong 0.26$, 0.40, and 0.55 fm^{-1}, which correspond to the maximum of $E1$, $E2$, and $E3$ form factors, respectively. Any appreciable $E4$ strength will result in an overestimation of the $E3$ strength at that excitation ener-

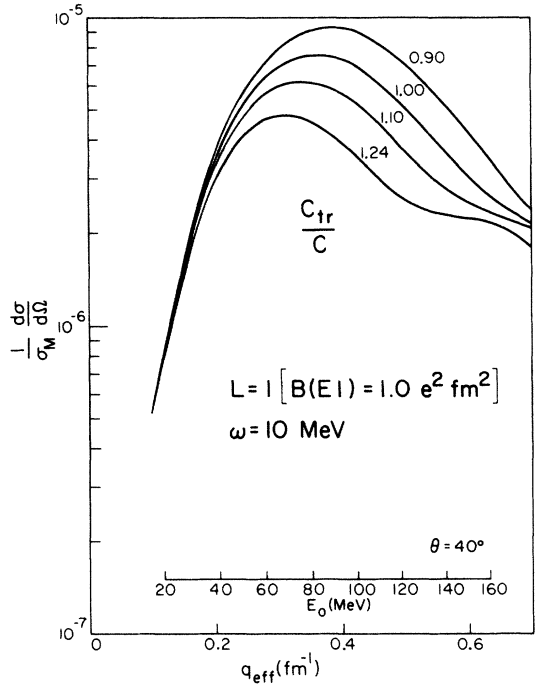

FIG. 8. The calculated Tassie-model dipole form factor per unit $B(E1)$ at $\omega = 10$ MeV for various c_{tr}/c_0, and thus various transition radii.

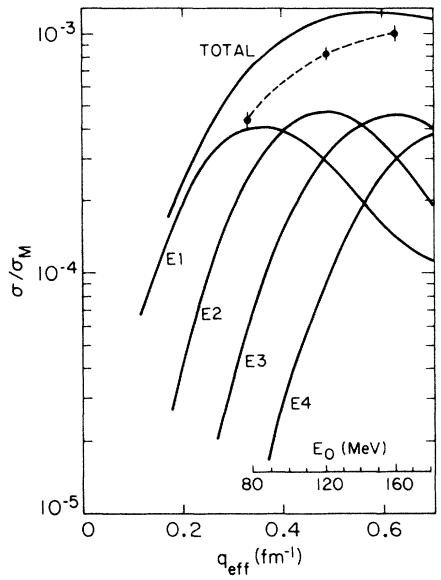

FIG. 9. Tassie model form factors for $E1$–$E4$, assuming a full sum rule of strength at $\omega = 10$ MeV for each multipole. The total form factor in this case peaks between the maximum of the $E2$ and $E3$ form factors. If higher multipoles were included, the total form factor would continue to rise. The points represent the experimental form factor for $5.5 \leq E_x \leq 6.5$ MeV at fission threshold (arbitrarily normalized) and the dashed line is a guide for the eye.

gy in a fit restricted to $\lambda \leq 3$. Figure 9 also shows the measured form factor, arbitrarily normalized, in the threshold region (5.5—6.5 MeV), a region previously considered to be dominated by 2^+ states. This form factor continues to rise even at high q, suggesting that there is a rather uniform fraction of sum rule strength in this region for all multipoles up to at least $E3$.

B. The QRPA

The random phase approximation (RPA) works well in describing the giant resonances microscopically.[44] For the case of uranium Zawischa and Speth[45] have calculated $E0$, $E1$, and $E2$ strength functions using the quasiparticle RPA (QRPA). This calculation includes 300 1p-1h states

TABLE III. The QRPA results. The numbers in parentheses refer to an exponent [e.g., 0.189(−3) is equivalent to 0.189×10^{-3}]. $B(E\lambda)$ values are in units of $e^2\text{fm}^{2\lambda}$, except for $B(E0)$, which has units $e^2\text{fm}^4$. The cross sections σ/σ_M are dimensionless and yield the QRPA form factors when divided by their corresponding $B(E\lambda)$ values. The 3^- and 4^+ states are rotational levels built on the 1^- and 2^+ resonances, respectively.

J^π	ΔT	K	ω (MeV)	$B(E\lambda,\omega)$ ($e^2\text{fm}^{2\lambda}$)	σ/σ_M (80.3 MeV)	σ/σ_M (118.4 MeV)	σ/σ_M (163.8 MeV)
0^+	0	0	1.41	6.0(2)	0.730(−5)	0.610(−5)	0.280(−5)
0^+	0	0	4.45	2.4(2)	0.210(−5)	0.130(−5)	0.158(−5)
0^+	0	0	6.44	1.7(2)	0.168(−5)	0.120(−5)	0.086(−5)
0^+	0	0	9.4	12.6(2)	0.196(−4)	0.265(−4)	0.143(−4)
0^+	0	0	14.9	37.6(2)	0.644(−4)	0.108(−3)	0.817(−4)
0^+	1	0	17.5	18.2(2)	0.275(−4)	0.457(−4)	0.323(−4)
0^+	1	0	23.7	39.6(2)	0.524(−4)	0.955(04)	0.726(−4)
1^-	1	0	11.3	26.3	0.189(−3)	0.142(−3)	0.661(−4)
1^-	1	1	12.7	34.1	0.288(−3)	0.246(−3)	0.108(−3)
2^+	0	2	1.16	45.2(2)	0.172(−3)	0.273(−3)	0.192(−3)
2^+	0	0	1.47	18.7(2)	0.530(−4)	0.640(−4)	0.290(−4)
2^+	0	1	3.08	5.0(2)	0.160(−4)	0.226(−4)	0.126(−4)
2^+	0	2	4.22	9.1(2)	0.330(−4)	0.510(−4)	0.320(−4)
2^+	0	0	4.4	7.8(2)	0.190(−4)	0.220(−4)	0.091(−4)
2^+	0	1	5.66	8.14(2)	0.250(−4)	0.349(−4)	0.175(−4)
2^+	0	0	6.47	5.0(2)	0.133(−4)	0.160(−4)	0.077(−4)
2^+	0	0	9.2	17.1(2)	0.447(−4)	0.667(−4)	0.380(−4)
2^+	0	1	10.4	34.8(2)	0.108(−3)	0.196(−3)	0.153(−3)
2^+	0	2	11.0	25.0(2)	0.829(−4)	0.163(−3)	0.142(−3)
2^+	0	0	14.6	3.39(2)	0.108(−4)	0.227(−4)	0.217(−4)
2^+	1	0	17.3	12.8(2)	0.288(−4)	0.458(−4)	0.266(−4)
2^+	1	1	19.7	24.5(2)	0.635(−4)	0.122(−3)	0.969(−4)
2^+	1	2	21.1	17.2(2)	0.481(−4)	0.103(−3)	0.957(−4)
2^+	1	0	23.7	11.1	0.129(−5)	0.540(−5)	0.114(−4)
3^-	1	0	11.3	21.6(3)	0.970(−6)	0.300(−5)	0.260(−5)
3^-	1	1	12.7	12.7(3)	0.150(−5)	0.235(−5)	0.290(−5)
4^+	0	2	1.16	12.9(5)			
4^+	0	0	1.47	46.5(5)			
4^+	0	1	3.08	10.5(5)			
4^+	0	2	4.22	0.84(5)			
4^+	0	0	4.4	21.5(5)			
4^+	0	0	6.47	2.0(5)			
4^+	0	0	9.2	20.4(5)			
4^+	0	1	10.4	31.7(5)			
4^+	0	2	11.0	7.7(5)			
4^+	0	0	14.6	0.71(5)			
4^+	1	0	17.3	27.0(5)			
4^+	1	1	19.7	35.5(5)			
4^+	1	2	21.1	4.5(5)			
4^+	1	0	23.7	0.11(5)			

and the corresponding 2p-2h combinations. The single-particle basis was derived using a modified Woods-Saxon potential with parameters fitted to ^{208}Pb data and modified for the ground state deformation in uranium using the results of Brack *et al.*[46] The inclusion of 2p-2h states provides a partial spreading width for the collective states. Without performing continuum RPA calculations, they could not reproduce the escape width of the resonances. Hence, for all comparisons with data, we must convolute the theoretical results with a phenomenological width.

Table III lists the results of the QRPA calculations for uranium. As predicted in simpler calculations like the cranking model,[47] not only the dipole, but also the quadrupole, states are split into their corresponding K components. In fact, since a prolate nucleus cannot sustain a purely radial (monopole) vibration, the $\lambda=2, K=0$ and $\lambda=0, K=0$ states are mixed, and give rise to $K=0$ states at 9 and 15 MeV. However, the mixing is slight and most of the isoscalar monopole strength resides at $E_x=15$ MeV and most of the isoscalar quadrupole strength lies at $E_x=10$ MeV.

The $E1$ strength calculated in the QRPA agrees well in strength and central energy with the photofission data of Saclay.[36] However, the QRPA does not produce a large enough K splitting in this case.

The QRPA gives the transition charge density for the collective $E0$, $E1$, and $E2$ states that we have used to calculate form factors and cross sections using FOUBESFIT. Electron scattering cross sections for the kinematics of the present experiment have been generated from the QRPA strength and form factors and are also listed. The transition charge densities of the QRPA for collective states are generally surface peaked like the Tassie model densities; however, they do show some contribution from the nuclear interior. Figure 10 demonstrates this fact for the two modes of the dipole resonance. The resulting cross sections as a function of q_{eff} in Fig. 10(c) have similar shapes. The $K=1$ mode peaks only slightly higher in q than the $K=0$ component.

Transition radii for the QRPA states are listed in Table IV. For all cases these radii do not differ significantly from those of unmodified ($c_{\text{tr}}/c_0=1$) Tassie transition densities. This gave us confidence that, in the subsequent analysis, permitting excursions in the ground state half-density radius by $\pm 10\%$ in calculating Tassie form factors more than amply encompasses the possible variations of the true $E\lambda$ form factors with excitation energy.[48]

Figure 11 shows the results of the QRPA calculations as compared to the angle-integrated cross section $4\pi a_0/\sigma_M$. Because the width of the states is not reproduced in the QRPA, we have spread each state into a Breit-Wigner shape with a full width at half maximum given by $\Gamma=0.28E_x$, a value suggested by (e,e') (Ref. 11) and (α,α') (Refs. 2 and 3) data on uranium. These cross sections were then multiplied by a parametrization of the $E1$ fission probability as a function of excitation energy deduced from (γ,f) (Refs. 36, 49, and 50) work. Figure 12 shows this fission probability. The large threshold peak arises from competition between fission and neutron emission 200 keV above fission threshold. The subsequent rises in the probability indicate the onset of second and

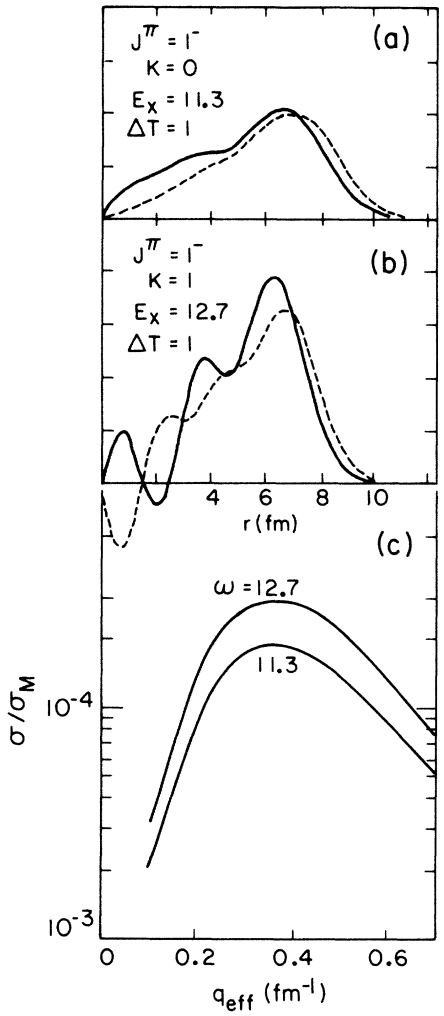

FIG. 10. The QRPA densities and form factors for the GDR. (a) and (b) show the transition charge densities for the $K=0$ and 1 modes, respectively. The solid line is the proton density and the dashed line is the negative of the neutron density. This difference in sign signifies an isovector resonance. (c) shows the resulting cross sections as a function of q_{eff}.

third chance fission. The curves of Fig. 11 agree reasonably with the data in both shape and magnitude. A few differences are worth noting, however. The 80 MeV spectrum falls below the theoretical curve in places, and shifting the central energy of the calculated peaks will not account for the difference. This is probably due to the fact that we find less $E2/E0$ strength than predicted by the QRPA. This deficiency, though present in the 118 MeV

TABLE IV. QRPA transition radii, calculated using Eq. (6), for the collective dipole and quadrupole states.

J^π	K	ΔT	R_{tr}^{λ}
1^-	0	1	1.03
1^-	1	1	0.96
2^+	1	0	0.98
2^+	2	0	0.95

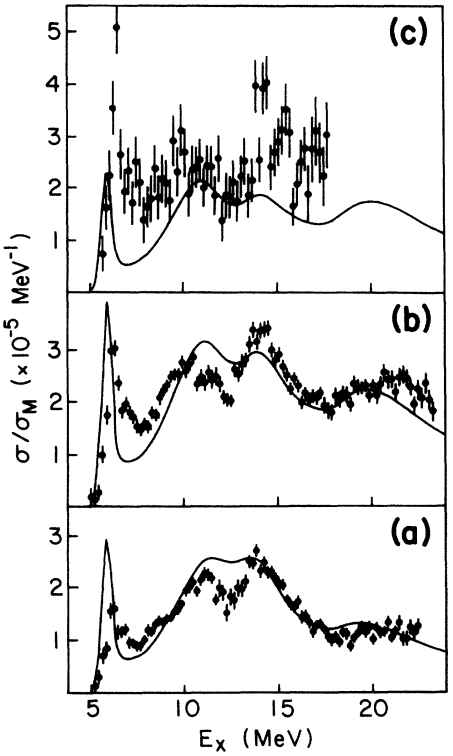

FIG. 11. Doubly differential ^{238}U(e,e′f) cross sections $d^2\sigma_f/\sigma_M d\Omega_{e'} d\omega$ (taken from the bottom panels in Figs. 4–6) at (a) 80.3, (b) 118.4, and (c) 163.8 MeV, compared to the QRPA calculations (solid lines) as described in the text.

spectrum also, is not as pronounced due to rising $E3$ contributions. The calculated cross sections at 160 MeV fall well below the data since contributions from $E3$ and higher order multipoles will be significant at this momentum transfer and the QRPA calculation did not include them.

The comparison of Fig. 11 is encouraging, but a more detailed comparison of theory and experiment is possible using the multipole decomposition presented in Sec. VI.

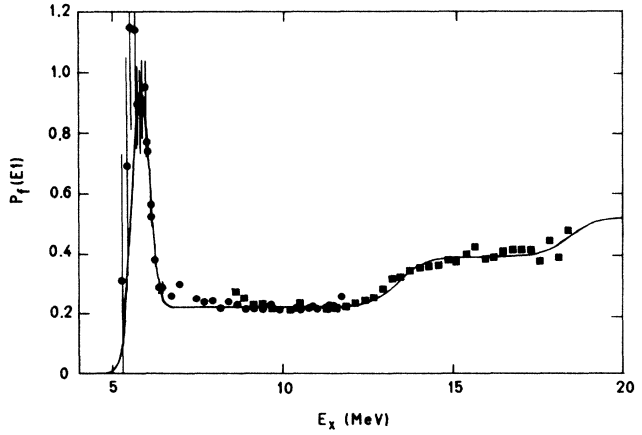

FIG. 12. The dipole fission probability $P_f(E1,\omega)$ deduced from Refs. 49 (dots) and 35 (squares) with our own parametrization of these data (solid line).

C. Sum rules

The general properties of the nuclear ground state[51] limits the total available energy-weighted transition strength. Under the simplest assumption that the nuclear Hamiltonian consists of a kinetic energy term and a potential which depends only on spatial coordinates, the electromagnetic energy-weighted sum rules are

$$S(E0)=\frac{2\hbar^2}{M}Z\langle r^2\rangle ,$$
$$S(E1)=\frac{9}{4\pi}\frac{\hbar^2}{2M}\frac{NZ}{A} , \tag{17}$$
$$S(E\lambda)=\frac{\lambda(2\lambda+1)^2}{4\pi}\frac{\hbar^2}{2M}Z\langle r^{2\lambda-2}\rangle \text{ for } \lambda\geq 2 ,$$

in which M is the nucleon mass, $\hbar$ is Planck's constant divided by 2π, and

$$\langle r^{2\lambda-2}\rangle=\int \rho_{tr}(r)r^{2\lambda}dr \Big/ \int \rho_{tr}(r)r^2dr$$

is the $(2\lambda-2)$th moment of the ground-state charge distribution for the nucleus with N neutrons, Z protons, and A nucleons. Weneser and Warburton[52] justify a division of the strength into isovector and isoscalar components $(N/A)S(E\lambda)$ and $(Z/A)S(E\lambda)$, respectively.

The sum rules listed in Table V were derived from the deformed nuclear ground state charge distribution measured by Cooper *et al.*[42] and Creswell.[43] Integration over the angular dependence results in a radial charge distribution which is used in calculating the moments of Eq. (17). These values are slightly larger than those calculated assuming a simple Fermi distribution with $c_0=6.805$ fm and $t=0.605$ fm.

VI. MULTIPOLE DECOMPOSITION

In order to understand the nature of our coincidence data in more detail, we have decomposed the coincidence spectra into multipoles using the model form factors calculated in Sec. V. The double-differential cross sections can be written as

$$\frac{1}{\sigma_M}\frac{d^2\sigma_f}{d\omega\, d\Omega_{e'}}=\sum_{\lambda=0}^{\infty}P_f(E\lambda,\omega)F^2(E\lambda,q,\omega)\frac{dB(E\lambda,\omega)}{d\omega} , \tag{18}$$

TABLE V. Calculated energy-weighted sum rule strengths. Here, $\langle r^{2\lambda-2}\rangle$ are moments of the ground state charge distribution in units of fm$^{2\lambda-2}$ deduced from Cooper *et al.* (Ref. 42) and Creswell (Ref. 43). $S(E\lambda)$ represents the full sum rule, whereas $S(E\lambda, \Delta T=0)$ is only the isoscalar part of the sum. The $E0$ sums have units MeV fm^4, whereas sums for the other multipoles have units MeV fm$^{2\lambda}$.

λ	$\langle r^{2\lambda-2}\rangle$	$S(E\lambda)$	$S(E\lambda, \Delta T=0)$
0		2.60×10^5	1.01×10^5
1		839 ($\Delta T=1$)	
2	34.1	2.59×10^5	1.00×10^5
3	1547	3.45×10^7	1.33×10^7
4	1.181×10^5	4.21×10^9	1.63×10^9
5	7.686×10^6	5.11×10^{11}	1.98×10^{11}

in which P_f is the fission probability which may depend on multipolarity $E\lambda$, F^2 is the nuclear form factor, and $dB/d\omega$ is the strength function for each multipole. Given model form factors F^2, one may fit the spectra and deduce $P_f(dB/d\omega)(E\lambda,\omega)$ for the most important multipoles, up to the number of different values of q measured.

In the present case we are limited to fitting only $E1$, $E0/E2$, and $E3$:

$$\frac{1}{\sigma_M}\frac{d^2\sigma_f}{d\omega\, d\Omega_{e'}} = P_f(E1,\omega)\frac{dB(E1,\omega)}{d\omega}F^2(E1,q,\omega) + \left[\tfrac{1}{2}P_f(E0,\omega)\frac{dB(E0,\omega)}{d\omega} + P_f(E2,\omega)\frac{dB(E2,\omega)}{d\omega}\right]F^2(E2,q,\omega)$$
$$+ P_f(E3,\omega)\frac{dB(E3,\omega)}{d\omega}F^2(E3,q,\omega)\ . \tag{19}$$

The combination of $E0$ and $E2$ strength results from the fact that for the low-q region the $E0$ form factor has the same shape as the $E2$ form factor with half the magnitude. In the Tassie model the ratio

$$F^2(E0,q,\omega)/F^2(E2,q,\omega) = 25/16\pi \cong \tfrac{1}{2}\ .$$

For the QRPA the ratio varies from 0.35 to 0.60 for the collective isoscalar $0^+,2^+$ states. The similarity in shape makes any separation of $E0$ and $E2$ strength by their q dependence impossible.

We term the decomposition performed with the present data at three values of q "unconstrained" since no special constraint is made on the magnitude or shape of the $E1$ contribution. On the other hand, the available photofission data can be included in the present analysis as a fourth data point with[53]

$$\sigma_{\gamma,f} = P_f(E1,\omega)\left[\frac{16\pi^3\alpha}{9}\omega\right]\frac{dB(E1,\omega)}{d\omega}\ . \tag{20}$$

We label this type of fit "constrained" because the photofission data overwhelmingly dominate the determination of the $E1$ strength function. Although it may appear obviously advantageous to make use of the information about the $E1$ distribution afforded by the photofission data, one must regard the results with caution: Even small errors in the absolute normalization of the (γ,f) data will produce large errors in the determination of the other strength functions.

In order to investigate the model dependence of the strength extraction, we have used Tassie model form factors with $c_{tr}/c_0 = 0.9$, 1.0, and 1.1. As has been mentioned, this should easily bracket the real variation in form factors, which in the low-q regime can only depend on R^{λ}_{tr}. For simplicity of notation, we shall refer to fits using a given set of form factors with the triplet $[(c_{tr}/c_0)E1, (c_{tr}/c_0)E2/E0, (c_{tr}/c_0)E3]$. To improve the accuracy of the extraction, we have integrated the data of Fig. 11 over 1 MeV intervals in excitation energy.

A. Constrained fits

In the case of the constrained fits, we were able to search the 27 combinations of transition radii for the best χ^2 using the photofission data of Saclay.[36] The data prefer an enlarged $E1$ radius and a reduced $E3$ radius, with the combination (1.1, 1.0, 0.9) yielding the best χ^2. The small $E3$ transition radius is easy to understand; since the 160 MeV data contain large contributions from $E4$ strength, the best fit to the data will be obtained for a model $E3$ form factor which peaks between the maximum of the actual $E3$ and $E4$ form factors, but moving the first maximum of the form factor out in momentum transfer is equivalent to reducing the transition radius. The magnitude, however, is also changed and the $E3$ strength is overestimated.

The large $E1$ transition radius suggests either that the absolute magnitude of the Saclay data is too large [since increasing c_{tr}/c_0 decreases the magnitude of the electron scattering form factor and thereby the $E1$ cross section per unit $B(E1)$], that the $E1$ data actually imply a larger radius, or that the longitudinal $E1$ matrix elements deduced in electron scattering are not as simply related to the transverse matrix elements of the photon work as Eq. (4) implies.

The first alternative is impossible to verify without independent measurements of each cross section involved. Although recent measurements of the photofission cross section from Giessen[54] agree with the data of Saclay[36] rather than the data set of Livermore[50] (which is consistently 20% larger in magnitude), there is perhaps some indication that the Giessen data lie systematically 5–10% below the Saclay results. Using the Giessen rather than the Saclay data in the multipole decomposition does not change the preference for an enlarged $E1$ transition radius. Regarding the absolute normalization of the electron scattering data, we have integrated the spectra over the interval $7 \le E_x \le 12$ MeV and compared our data and the Illinois data[21] on a common plot versus q_{eff}. The data sets are in general agreement with ours, tending to be $\sim$20% higher. Nevertheless, the two experiments were performed at very different energies and angles, and in the DWBA the experimental form factors are not functions solely of q_{eff}, but of the kinematical variables as well. Thus such a difference in no way necessarily implies a discrepancy. Indeed, there is real hope that strength functions and transition radii will be determined precisely through a more extensive data set in q.

The second alternative contradicts the work of Danos and Okamoto,[55] which predicts an increased radius $c_{tr}/c_0 = 1.24$ for the $K=0$ state of the dipole and a decreased radius $c_{tr}/c_0 = 0.9$ for the $K=1$ state.[11] Since the $K=1$ state contains twice the strength of the $K=0$ state,

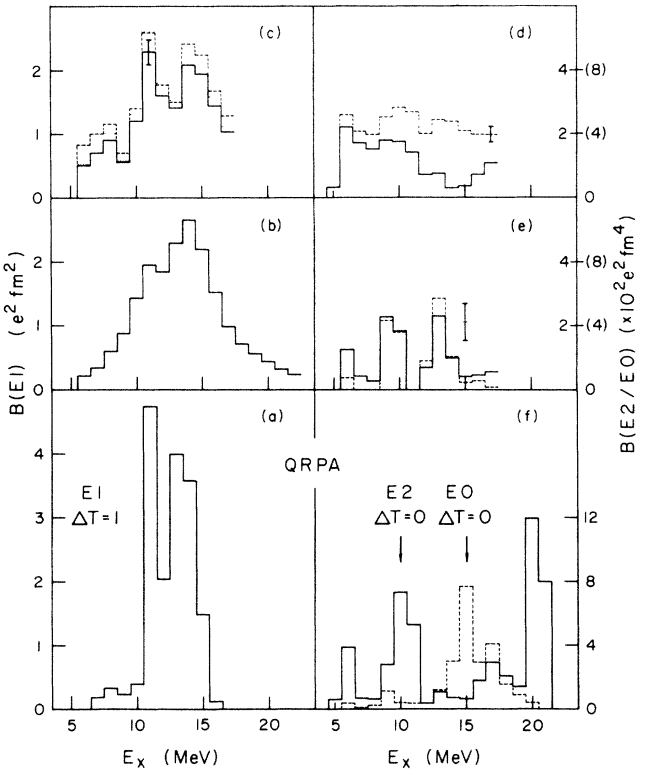

FIG. 13. Experimental and theoretical strength functions integrated over intervals of 1 MeV excitation energy. (a) $E1$, QRPA; (b) $E1$, photofission data from Ref. 35; (c) $E1$, this work, unconstrained fits with $[(c_{tr}/c_0)^{E1}, (c_{tr}/c_0)^{E2/E0}, (c_{tr}/c_0)^{E3}]=(0.9, 0.9, 0.9)$ (solid curve), (1.0, 1.0, 0.9) (dashed curve), (1.1, 1.0, 0.9) (dotted curve); (d) $E2/E0$ constrained fits with (1.1, 1.0, 0.9) (solid curve) and (1.0, 1.0, 1.0) (dashed curve); (e) $E2/E0$ unconstrained fits, key as in (c)—inner (outer) scale for $E2$ ($E0$); (f) $E2$ (solid line), $E0$ (dashed line), QRPA. The QRPA results are multiplied by the $E1$ fission probability. Error bars indicate statistical errors only.

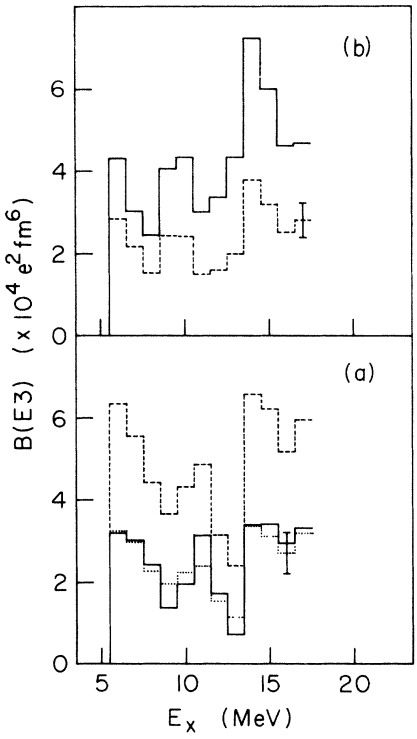

FIG. 14. Experimental $E3$ strength functions for (a) unconstrained and (b) constrained fits using the transition radii of Figs. 11(e) and 11(d), respectively.

the weighted average $c_{tr}/c_0 \cong 1.0$. However, the cross sections themselves do not agree with the Danos conclusion. If we calculate the 80.3 MeV $E1$ contribution to the electron cross section using the Saclay data and the $K=0$ and 1 form factors with the modified radii $c_{tr}/c_0=1.24$ and 0.9, respectively, the electron scattering data are overpredicted by at least 10% at 14 MeV.

The third possibility stems from the fact that electron-scattering experiments do seem to show $E1$ strength below $E_M=10$ MeV, which is not seen in the real photon data. We shall discuss this in more detail in the next section.

Figures 13(d) and 14(b) show the resulting strength extraction for the constrained data for two combinations of transition radii. Because of the strong influence which the photofission data exerts on the fit, the deduced $E2$ strength varies wildly as $(c_{tr}/c_0)^{E1}$ varies. The extracted $E1$ strength, on the other hand, agrees with the Saclay result simply by the nature of the fit. The strength function labeled "$E3$" represents an upper limit to the actual $E3$ distribution, since it contains the strength of all higher multipoles as well.

B. Unconstrained fits

The same 27 combinations of transition radii have been used in the unconstrained fits. The fits for a few of these combinations are shown in Figs. 13(c), 13(e), and 14(a). In this case, we have no χ^2 to guide us in choosing the best solution. We therefore have demanded that the fit reproduce the $E1$ strength function as best as possible. Being guided by the QRPA transition radii for collective states (all near $c_{tr}/c_0=1.0$), we believe the combination (1.0, 1.0, 0.9) to be best, with the reduced $E3$ transition radius resulting from $E4$ contributions as discussed earlier.

Encouragingly, the extracted strength function for $E1$ agrees extremely well with the photofission results. At low energy (5—7 MeV) the electron scattering yields more strength than the photofission result. This has been noted in (e,e') experiments on lead[56] and nickel,[57] but its cause is not understood. Sasao and Torizuka[56] claim that the discrepancy perhaps results from a problem with their form factor in this region. Although the present experiment does not offer an explanation for this $E1$ discrepancy, it does imply that the structures in the (e,e') data are not due to background in the singles spectrum.

Figures 13(a) and 13(f) show the QRPA predictions for $E1$, $E0$, and $E2$. Although the calculated $E1$ strength distribution is not broad enough, the energy-weighted strength agrees with the Saclay results. The $E2/E0$ re-

sults suggest a concentration of $E2$ strength at 10 MeV and a concentration of $E0$ strength at 15 MeV. These energies correspond closely to the locations of the peaks we see in our extracted (unconstrained) $E2/E0$ spectrum.

The $E3$ spectrum of Fig. 14 shows a few interesting features. The threshold bump due to the fission probability is evident at 6 MeV and a significant rise near 13 MeV is probably due to second chance fission. The peak at 10 MeV shows up at roughly the position at which various RPA calculations[58] on ^{208}Pb predict a large collective $E4$ state. Without this bump at 10 MeV, the spectrum is consistent with the low energy octupole resonance at 5 MeV and the high energy octupole resonance at 15 MeV.

VII. COMPARISONS TO OTHER DATA

Table VI lists the extracted energy-weighted strengths for various combinations of transition radii in units of the sum rules of Sec. V. For the $E2/E0$ determination, assuming that everything below 11 MeV is isoscalar $E2$ strength, and that from 11 to 17 MeV is isoscalar $E0$ strength, we obtain a reasonable fraction of the sum rule exhausted for the monopole, given a normal (i.e., the $E1$) fission probability, in keeping with the alpha-scattering results. The amount of $E2$ strength, no matter what combination of transition radii is considered, is consistently lower (by at least a factor of 2), assuming normal fission probability, than either QRPA or sum-rule estimates (see Table VI). Though we cannot determine whether this indicates missing $E2$ strength or a reduced $E2$ fission probability, our results are not inconsistent with the KVI $(\alpha,\alpha' f)$ measurements[5–8] at $E_\alpha = 120$ MeV which claim an anomalously low fission probability for the quadrupole resonance. An Oak Ridge collaboration[4] found in a similar experiment, however, that the quadrupole resonance fissions with roughly the same probability as the nuclear continuum ($\simeq$22%). Because this measurement was made at a different energy, $E_\alpha = 152$ MeV, and at a single, special angle of fission decay (in the momentum transfer direction), we find it difficult to compare these results with our own or the KVI work.

Figure 15 shows our preferred estimate for the $E2/E0$ differential strength function $dB/d\omega$ in 200 keV bins, with $c_{tr}/c_0 = (1.0, 1.0, 0.9)$. The hatched area corresponds to the extracted $E2/E0$ strength from a similar (e,e'f) experiment at the University of Illinois.[21] However, that experiment covered only a slightly smaller range of momentum transfer. Those data were fitted to $E1$ and $E2/E0$ only, using the Saclay photofission data to constrain the fit. Since their cross sections for ω between 5 and 12 MeV are, at worst, 20% smaller in magnitude than ours when plotted smoothly versus q_{eff}, their larger $E2/E0$ strength can be accounted for by $E3$ contributions to their spectrum in a similar way as our $E3$ distribution contains contributions from $E4$.

Figure 15 extends to 23 MeV even though the 160 MeV data did not reach that excitation energy. These data were added from the unconstrained fit (1.0, 1.0, 0.9) in this region where the contribution from the dipole is less important. The peak near 22 MeV probably corresponds

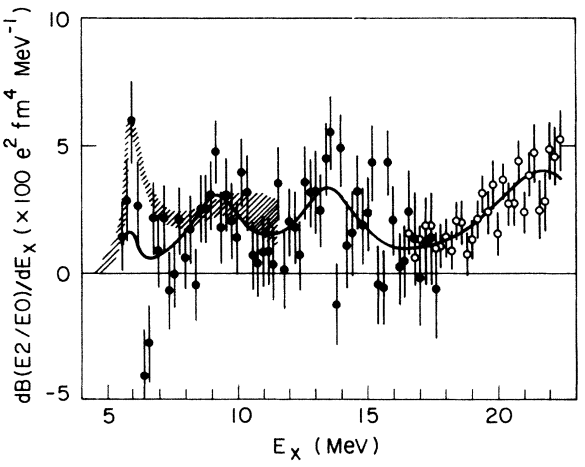

FIG. 15. Experimental $E2/E0$ strength function for (1.0, 1.0, 0.9) with 200 keV resolution. The dots come from the unconstrained fit and the open circles from the constrained fit in the region above 17 MeV, where the $E1$ contribution is small and no 163.8 MeV data exist. The solid line is the best fit to Breit-Wigner resonances modified by $P_f(E1,\omega)$ (see Table VII). The shaded region is the strength function deduced in Ref. 21.

to the isovector $E2$ strength expected in this region and observed in (e,e') (Ref. 11) to lie at 21.5 MeV and to exhaust 50–70% of the isovector sum rule. Assuming a Breit-Wigner shape to the line, our data account for roughly 70% of the isovector $E2$ EWSR. Table VII lists the results of a parametrized fit to the extracted strength functions for $c_{tr}/c_0 = (1.0, 1.0, 0.9)$. Although the data do not necessarily resolve into pure Breit-Wigner shapes, this table gives some indication where the strength is concentrated. The extracted sum rule strengths from the resonance parameters are slightly larger than the values deduced directly from the data.

In general, the location of strength in the (e,e') experiment[11] agrees with our own determinations. However, Pitthan *et al.* have not fitted their data, which span approximately the same region of momentum transfer as the present data, to $E0$ strength. In addition, they have chosen the transition radii $c_{tr}/c_0 = 1.24$ and 0.9 for the two modes of the dipole. Our data do not support these radii. The strength which we attribute to the isoscalar monopole vibration lies beneath the upper lobe of the dipole. If we neglect the monopole, attribute the cross section around 14 MeV to the dipole only, and use a form factor which is too large (e.g., $c_{tr}/c_0 = 0.9$), we deduce the same $B(E1)$ as if we considered some of the cross section to be due to $E0$ and used a smaller form factor (e.g., $c_{tr}/c_0 = 1$) to derive the $E1$ strength. This may explain the good agreement Pitthan *et al.*[11] achieved with the real photon data even though they use a form factor which we believe to be incorrect. Interestingly, the (e,e') measurements do not find a full sum rule of isoscalar quadrupole strength, but for unmodified Tassie model form factors see only 40% of the isoscalar sum rule. This is not inconsistent with our results.

TABLE VI. Percent exhaustion of energy-weighted sum rules by multipolarity. Except for $E1$, and where noted, all strengths are reported relative to the isoscalar energy-weighted sum rules, EWS_0R. Numbers cited in parentheses refer to strength seen in the fission channel numbers; those without parentheses refer to total strengths. For the present work, these result from assuming $P_f(E1)$ for each multipole. The $E3$ EWS_0R fractions represent upper limits only. Numbers in square brackets refer to the parameters $[E_x, \Gamma]$ obtained in a fit of the data to a resonance line shape.

	E_x (MeV)	$E1$	$E0$	$E2$	$E3$	Ref.
QRPA	5.5–17.5[a]	87	66	84		45
(γ,tot)	5.5–17.5[a]	88				36
(α,α')	[9.3, 2]		30			2
	[13.7, 3]		65			
	[10.8, 3]			66[b]		
($\alpha,\alpha' f$)	[9.3, ~3]			(3.5) 16		5–8
($\alpha,\alpha' f$)	[10.6, 2.2]		150[c]	50[c]		4
			100[d]	75[d]		
($\alpha,\alpha' f$)	7–16		80[e]			10
(e,e')	[9.9, 2.9]			38[f]		11
				77[g]		
	[10.8, 3.2]	36[h]				
	[13.9, 4.5]	81[i]				
	[21.6, 5.0]			51[f,j]		
	[28.4, 8.1]				91[f,j]	
(e,e'f)	5.7–7.0			(3.7)8[k]		21
	7.0–11.7			(10) 45[k]		
(e,e'f)	<6.5[l]			(0.9±0.4) 13		Present
				(1.0±0.4) 15		work
				(1.1±0.4) 17		
	<17.5[l]	82±4	(41±4) 148[m]	(21±2) 74[n]	(24±1) 76	
		80±4	(48±6) 168[m]	(24±3) 84[n]	(29±2) 94	
		88±4	(61±4) 212[m]	(30±2) 106[n]	(27±2) 86	
	<11[l]			(6.7±1.0) 30		
				(7.9±1.2) 33		
				(9.3±1.0) 39		
	11.0–17.5[l]		(28±4) 88			
			(32±5) 102			
			(42±4) 132			
	<6.5[o]			(1.5±0.2) 2.2		
				(1.5±0.2) 2.3		
	<17.5[o]	87±0.4	(39±2) 140[m]	(20±1) 70[n]	(31±1) 101	
		87±0.4	(63±2) 221[m]	(32±1) 111[n]	(26±2) 84	
	<12[o]			(10.7±0.4) 44		
				(14.1±0.4) 59		
	12–17.5[o]		(18±2) 52			
			(35±2) 103			

[a]Limited to the excitation range of the present experiment.
[b]$L=4$ assignment is also consistent with the data.
[c]Assumes complete K mixing.
[d]Assumes K conservation.
[e]$E_x \sim 12.5$, $\Gamma \sim 6$ after correction for $P_f(E1)$.
[f]$c_{tr}/c_0 = 1.0$.
[g]$c_{tr}/c_0 = 1.1$.
[h]$c_{tr}/c_0 = 1.24$.
[i]$c_{tr}/c_0 = 0.9$.
[j]With respect to the isovector sum rule.
[k]Only $E1$, $E2/E0$ included in fit.
[l]Fit unconstrained by the photofission data. The three rows correspond to $c_{tr}/c_0 = (1.0, 0.9, 0.9)$ $(1.0, 1.0, 0.9)$, and $(1.1, 1.0, 0.9)$, respectively.
[m]Assumes all $E2/E0$ strength is $E0$.
[n]Assumes all $E2/E0$ strength is $E2$.
[o]Fit constrained by the photofission data. The two rows correspond to $c_{tr}/c_0 = (1.0, 1.0, 0.9)$ and $(1.1, 1.0, 0.9)$, respectively.

TABLE VII. Fit of the extracted strength distributions to Breit-Wigner line shapes modified by the $E1$ fission probability. The first set of six resonances comes from the unconstrained results with $c_{tr}/c_0 = (1.0, 1.0, 0.9)$. The second set of seven resonances comes from the constrained fits with the same set of transition radii. Because these parameters only indicate trends in the data rather than precise determinations of resonance parameters, we give no error bars. The strengths cited in percentages are given with respect to the energy-weighted sum rule of the appropriate ΔT.

$E\lambda$	E_x (MeV)	Γ (MeV)	Area	χ^2/ν	% EWSR	ΔT
$E1$	11.0	2.4	33	1.17	43	1
$E1$	14.5	5.0	36		62	1
$E2$	9.2	2.4	48×10^2	1.26	44	0
$E0$	13.2	2.8	44×10^2		116	0
$E3$	9.3	4.4	77×10^4	1.96	54	0
$E3$	16.1	6.3	76×10^4		92	0
$E1$	11.0	2.5	30	17.3	39	1
$E1$	14.0	3.7	39		65	1
$E2$	8.3	4.3	42×10^2	1.37	35	0
$E0$	10.8	5.5	39×10^2		84	0
$E2$	21.7	4.6	52×10^2		71	1
$E3$	9.6	4.6	85×10^4	1.85	61	0
$E3$	15.7	6.3	90×10^4		106	0

VIII. CONCLUSIONS

The data presented constitute some of the first results from coincident electron scattering experiments. Such measurements are plagued neither by the large radiative tail nor non-target-related backgrounds, both of which limit the accuracy of (e,e') singles measurements. The present data realize the expectation that broad overlapping continuum strength of different multipoles may be separated. Nevertheless, our strength extractions are somewhat model dependent due to the truncation of data in q; this truncation obviously most affects the highest multipoles incorporated into the fit.

The $E1$ distribution agrees well with that determined from photofission work, except for the discrepancy in the region around 8 MeV, where the present data show strength not seen in real photon work. A similar situation exists in (e,e') on ^{208}Pb and ^{58}Ni, and thus strongly indicates that the effect is not an artifact, but is physical in origin. Large differences in the transition radii corresponding to the $K=0,1$ modes of the GDR suggested in Ref. 11 are excluded. The isotropy of the fission fragment angular distribution above $E_x = 10$ MeV and particularly where the K substates of the isovector dipole resonance are well separated confirms that K is not conserved in the descent from saddle to scission.

$E3$ and higher multipoles are significant throughout the excitation energy range studied. The rise at threshold of the $E3$-and-higher strength distribution is probably due to the low energy octupole resonance (LEOR), while a narrow structure around 10 MeV could correspond to a collective $\Delta T=0$ $E4$ state. RPA calculations in^{208}Pb have shown such a state at that energy.

While the $E2/E0$ strength function shows considerable sensitivity to the choice of model form factors, resonances at 9.5 and 13 MeV are obvious under any variation. Associating the upper with the GM_0R (isoscalar GMR) yields good agreement both in position and strength ($\approx 100\%$ of the isoscalar $E0$ sum rule) with the monopole resonance predicted in QRPA and seen in $(\alpha,\alpha' f)$. On the other hand, the GQ_0R (isoscalar GQR) at 9.5 MeV is certainly missing strength, accounting for only $\frac{1}{2}-\frac{1}{3}$ of the QRPA prediction of 84% of the EWS_0R (isoscalar EWSR) in that state. Nevertheless, this is considerably more than the upper limits set by the KVI $(\alpha,\alpha' f)$ measurements. A suppression of the strength in the fission channel could either be due to a dynamical inhibition of the fission mode associated with this particular vibration, or markedly enhanced nonstatistical neutron decay, again specific to the quadrupole vibration. Either of these would be very surprising, and thus this problem must be considered one of the outstanding puzzles in giant resonance studies today. A direct measurement of the branching ratio Γ_n/Γ_f (rather than Γ_f/Γ_{tot} which is usually measured) and the neutron decay spectrum has been performed and is being analyzed.[59]

ACKNOWLEDGMENTS

We thank H. A. Schwettman, T. I. Smith, R. E. Rand, M. S. McAshan, J. T. Turneaure, and C. M. Lyneis for the accelerator operation, J. Garibaldi and A. Combs III of Lawrence Livermore National Laboratory for technical support, D. Zawischa and J. Speth for supplying us with their QRPA results on uranium, and S. Brain and J. T. Hoeksema for computer assistance on the data analysis. This work was supported in part by a National Science Foundation Graduate Fellowship (P.J.C.) and an Alfred P. Sloan Foundation Fellowship (K.V.B.), and by the Alexander von Humboldt Stiftung (K.T.K.).

*Present address: Fysisch Laboratorium, Rijksuniversiteit Utrecht, Postbus 80.000, 3508TA Utrecht, The Netherlands.
†Permanent address: Max-Planck-Institut für Kernphysik, D-6900 Heidelberg 1, Federal Republic of Germany.

[1]F. E. Bertrand, Annu. Rev. Nucl. Sci. **26**, 457 (1976); Nucl. Phys. **A354**, 129c (1981).
[2]H. P. Morsch, M. Rogge, P. Turek, C. Mayer-Böricke, and P. Decowski, Phys. Rev. C **25**, 2939 (1982).
[3]H. P. Morsch, M. Rogge, P. Turek, P. Decowski, L. Zemlo, C. Mayer-Böricke, S. A. Martin, G. P. A. Berg, I. Katayama, J. Meissburger, J. G. M. Römer, J. Reich, P. Wucherer, and W. Bräutigam, Phys. Lett. **119B**, 311 (1982).
[4]F. E. Bertand, J. R. Beene, C. E. Bemis, Jr., E. E. Gross, D. J. Horen, J. R. Wu, and W. P. Jones, Phys. Lett. **99B**, 213 (1981).
[5]J. van der Plicht, M. N. Harakeh, A. van der Woude, P. David, and J. Debrus, Phys. Rev. Lett. **42**, 1121 (1979).
[6]J. van der Plicht, M. N. Harakeh, A. van der Woude, P. David, J. Debrus, H. Janszen, and J. Schulze, Nucl. Phys. **A346**, 349 (1980).
[7]J. van der Plicht, M. N. Harakeh, A. van der Woude, P. David, J. Debrus, H. Janszen, and J. Schulze, Nucl. Phys. **A369**, 51 (1981).
[8]R. DeLeo, M. N. Harakeh, S. Micheletti, J. van der Plicht, A. van der Woude, P. David, and H. Janszen, Nucl. Phys. **A373**, 509 (1982).
[9]H. P. Morsch, M. Rogge, P. Decowski, H. Machner, C. Sükösd, P. David, J. Debrus, J. Hartfiel, H. Janszen, and J. Schulze, Phys. Lett. **119B**, 315 (1982).
[10]S. Brandenburg, R. DeLeo, A. G. Drentje, M. N. Harakeh, H. Janszen, and J. van der Woude, Phys. Rev. Lett. **49**, 1687 (1982).
[11]R. Pitthan, F. R. Buskirk, W. A. Houk, R. W. Moore, Phys. Rev. C **21**, 28 (1980).
[12]J. D. T. Arruda-Neto, S. B. Herdade, B. S. Bhandari, and I. C. Nascimento, Phys. Rev. C **14**, 1499 (1976).
[13]A. C. Shotter, D. Branford, J. C. McGeorge, and J. M. Reid, Nucl. Phys. **A290**, 55 (1977).
[14]J. D. T. Arruda-Neto, S. B. Herdade, B. S. Bhandari, and I. C. Nascimento, Phys. Rev. C **18**, 863 (1978).
[15]J. Aschenbach, R. Haag, and H. Krieger, Z. Phys. A **292**, 285 (1979).
[16]J. D. T. Arruda-Neto and B. L. Berman, Nucl. Phys. **A349**, 483 (1980).
[17]H. Ströher, R. D. Fischer, J. Drexler, K. Huber, U. Kneissl, R. Ratzek, H. Ries, W. Wilke, and H. J. Maier, Phys. Rev. Lett. **47**, 318 (1981).
[18]H. Ströher, R. D. Fischer, J. Drexler, K. Huber, U. Kneissl, R. Patzek, H. Ries, W. Wilke, and H. J. Maier, Nucl. Phys. **A378**, 237 (1982).
[19]J. G. Woodworth, D. Rowley, J. D. T. Arruda-Neto, P. J. Countryman, K. A. Griffioen, D. H. H. Hoffmann, K. T. Knöpfle, K. Van Bibber, M. R. Yearian, and J. R. Calarco, Phys. Lett. **153B**, 226 (1985).
[20]D. S. Onley and F. Zamani-Noor, private communication.
[21]D. H. Dowell, L. S. Cardman, P. Axel, G. Bolme, and S. E. Williamson, Phys. Rev. Lett. **49**, 113 (1982); D. H. Dowell, Ph.D. thesis, University of Illinois, 1981.
[22]K. A. Griffioen, P. J. Countryman, K. T. Knöpfle, K. Van Bibber, M. R. Yearian, J. G. Woodworth, D. Rowley, and J. R. Calarco, Phys. Rev. Lett. **53**, 2382 (1984); K. A. Griffioen, Ph.D. thesis, Stanford University, 1984.
[23]Other decay modes such as (e,e′α) are negligible. See, e.g., D. H. Dowell, P. Axel, and L. S. Cardman, Phys. Rev. C **18**, 1550 (1978).
[24]W. E. Kleppinger and J. D. Walecka, Ann. Phys. (Leipzig) **146**, 349 (1983).
[25]Polar angles θ measured with respect to the z axis are identical in both. However, the azimuthal angle ϕ, measured from the x axis toward the y axis, differs by 90°.
[26]T. W. Donnelly and J. D. Walecka, Annu. Rev. Nucl. Sci. **25**, 329 (1975).
[27]J. D. T. Arruda-Neto, S. B. Herdade, and I. C. Nascimento, Nucl. Phys. **A334**, 297 (1980).
[28]E. E. Chambers and R. Hofstadter, Phys. Rev. **103**, 1454 (1956).
[29]T. I. Smith, in *Physics of Quantum Electronics*, edited by S. F. Jacobs *et al.* (Addison-Wesley, Reading, Mass., 1981), Vol. 8.
[30]K. L. Brown, Stanford Linear Accelerator Center Report No. 75, July 1967 (unpublished).
[31]J. D. T. Arruda-Neto, R. Avida, J. R. Calarco, K. A. Griffioen, D. H. H. Hoffmann, K. T. Knöpfle, K. Van Bibber, R. Westervelt, and J. G. Woodworth, Nucl. Instrum. Methods **190**, 203 (1981).
[32]L. C. Maximon, Rev. Mod. Phys. **41**, 193 (1969).
[33]H. L. Crannell, Ph.D. thesis, Stanford University, 1964.
[34]P. R. Bevington, *Data Reduction and Error Analysis for the Physical Sciences* (McGraw-Hill, New York, 1969).
[35]A. Bohr, in *Conference on Peaceful Uses of Atomic Energy (Geneva)* (The United Nations, New York, 1956), Vol. 2, p. 151.
[36]A. Veyssière, H. Beil, R. Bergère, P. Carlos, A. Lepretre, and K. Kernbath, Nucl. Phys. **A199**, 45 (1973).
[37]R. Vandenbosch and J. R. Huizenga, *Nuclear Fission* (Academic, New York, 1973).
[38]J. Heisenberg, Adv. Nucl. Phys. **12**, 61 (1981).
[39]M. Goldhaber and E. Teller, Phys. Rev. **74**, 1046 (1948).
[40]L. J. Tassie, Aust. J. Phys. **9**, 407 (1956).
[41]G. R. Satchler, Part. Nucl. **5**, 105 (1973).
[42]T. Cooper, W. Bertozzi, J. Heisenberg, S. Kowalski, W. Turchinetz, C. Williamson, L. Cardman, S. Fivozinsky, J. Lightbody, Jr., and S. Penner, Phys. Rev. C **13**, 1083 (1976).
[43]C. Creswell, Ph.D. thesis, Massachusetts Institute of Technology, 1975.
[44]K. Goeke and J. Speth, Annu. Rev. Nucl. Sci. **32**, 65 (1982).
[45]D. Zawischa, J. Speth, and D. Pal, Nucl. Phys. **A311**, 445 (1978); in *The Dynamics of Nuclear Fission and Related Collective Phenomena*, Vol. 158 of *Lecture Notes in Physics*, edited by P. David, T. Meyer-Kukuck, and A. van der Woude (Springer, Berlin, 1982), p. 231; and private communication.
[46]M. Brack, T. Ledergerber, H. C. Pauli, and A. S. Jensen, Nucl. Phys. **A234**, 185 (1974).
[47]Y. Abgrall, B. Morand, E. Caurier, and B. Grammaticos, Nucl. Phys. **A346**, 431 (1980).
[48]Certainly if the QRPA correctly predicted the $E1$ K splitting, the corresponding transition radii may deviate further from the unmodified Tassie radii. However (see Sec. VI), our data at 80 MeV, in conjunction with the photofission data, do not support the assumption of larger variations in c_{tr}/c_0.
[49]P. A. Dickey and P. Axel, Phys. Rev. Lett. **35**, 501 (1975).
[50]J. T. Caldwell, E. J. Dowdy, B. L. Berman, R. A. Alvarez, and P. Meyer, Phys. Rev. C **21**, 1215 (1980).
[51]A. Bohr and B. R. Mottelson, *Nuclear Structure* (Benjamin, Reading, Mass., 1973), Vol. 2, p. 403.
[52]J. Weneser and E. K. Warburton, in *The Role of Isospin In Nuclear Physics*, edited by D. H. Wilkinson (North-Holland, Amsterdam, 1969).
[53]P. Axel, in *A Festschrift for Maurice Goldhaber*, edited by G.

Feinberg *et al.* (New York Academy of Sciences, New York, 1980).
[54]H. Ries, G. Mank, J. Drexler, R. Heil, K. Huber, U. Kneissl, R. Ratzek, H. Ströher, T. Weber, and W. Wilke, Phys. Rev. C **29**, 2346 (1984).
[55]M. Danos, Nucl. Phys. 5, 264 (1958); K. Okamoto, Phys. Rev. **110**, 143 (1958).
[56]M. Sasao and Y. Torizuka, Phys. Rev. C **15**, 217 (1977).
[57]R. Klein, Y. Kawozoe, P. Grabmayr, G. J. Wagner, J. Friedrich, and N. Voegler, Phys. Lett. **145B**, 25 (1984).
[58]P. Ring and J. Speth, Nucl. Phys. **A235**, 315 (1974).
[59]P. J. Countryman, private communication.

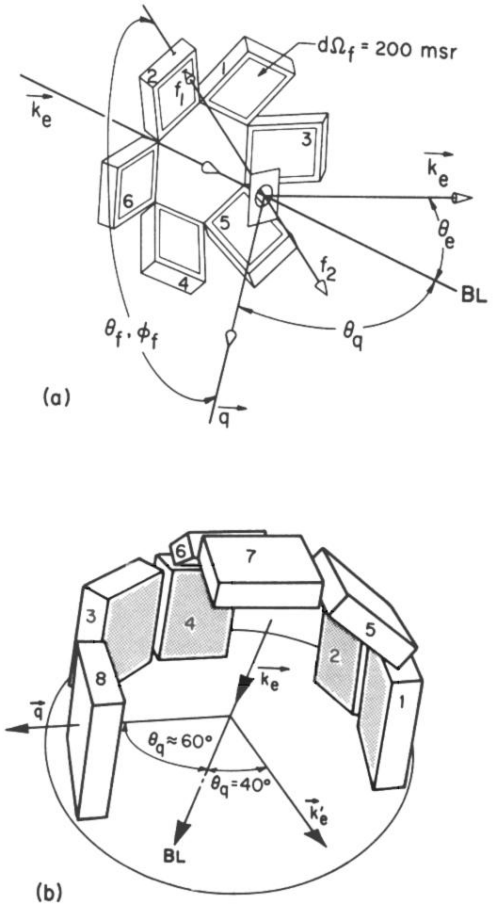

FIG. 1. The PPAC configurations used in the present experiment, for (a) the first and third runs, and (b) the second run.